Title
Two-photon production of pion pairs

Permalink
https://escholarship.org/uc/item/0vx433mf

Journal
Physical Review D, 42(5)

ISSN
2470-0010

Authors
Boyer, J
Butler, F
Gidal, G
et al.

Publication Date
1990-09-01

DOI
10.1103/physrevd.42.1350

PHYSICAL REVIEW D VOLUME 42, NUMBER 5 1 SEPTEMBER 1990

Two-photon production of pion pairs

J. Boyer,[a] F. Butler,[b] G. Gidal, G. Abrams, D. Amidei,[c] A. R. Baden,[d] M. S. Gold,
L. Golding,[e] G. Goldhaber, J. Haggerty,[f] D. Herrup,[g] I. Juricic,[a] J. A. Kadyk,
M. E. Levi, M. E. Nelson,[h] P. C. Rowson,[a] H. Schellman,[g] W. B. Schmidke,
P. D. Sheldon,[i] G. H. Trilling, and D. R. Wood[j]
Lawrence Berkeley Laboratory and Department of Physics, University of California, Berkeley, California 94720

T. Barklow, A. Boyarski, P. Burchat,[k] D. L. Burke, D. Cords, J. M. Dorfan,
G. J. Feldman, L. Gladney,[l] G. Hanson, K. Hayes, R. J. Hollebeek,[l] W. R. Innes,
J. A. Jaros, D. Karlen,[m] A. J. Lankford, R. R. Larsen, B. W. LeClaire,[j]
N. S. Lockyer,[l] V. Lüth, R. A. Ong,[c] M. L. Perl, B. Richter,
K. Riles, and J. M. Yelton[n]
Stanford Linear Accelerator Center, Stanford University, Stanford, California 94305

T. Schaad[o]
Harvard University, Cambridge, Massachusetts 02138

(Received 27 March 1990)

We present a new high-statistics measurement of the cross section for the process $e^+e^- \rightarrow e^+e^-\pi^+\pi^-$ at a center-of-mass energy of 29 GeV for invariant pion-pair masses $M(\pi^+\pi^-)$ between 350 MeV/c^2 and 1.6 GeV/c^2. We observe the $f_2(1270)$ and measure its radiative width to be $3.15\pm0.04\pm0.39$ keV. We also observe an enhancement in the $\pi^+\pi^-$ spectrum near 1 GeV. General agreement is found with unitarized models of the $\gamma\gamma\rightarrow\pi^+\pi^-$ reaction that include final-state interactions.

I. INTRODUCTION

Several experiments have reported measurements of the reaction

$$e^+e^- \rightarrow e^+e^-\pi^+\pi^- \ . \qquad (1)$$

In the resonance region the reaction is dominated by the formation of the $f_2(1270)$ and its interference with the Born continuum. Reasonably consistent measurements[1-12] of the radiative width $\Gamma(f_2(1270)\rightarrow\gamma\gamma)$ have been obtained. The mass region below the $f_2(1270)$ has however been a source of some confusion. In particular, the expected 0^{++} state, $f_0(975)$, has never been observed in $\gamma\gamma$ interactions, the best limits being from JADE,[5] $\Gamma(f_0(975)\rightarrow\gamma\gamma)<0.8$ keV, and from Crystal Ball,[9] $\Gamma(f_0(975)\rightarrow\gamma\gamma)<1.0$ keV. Near threshold, the PLUTO, DM1, and DM2 Collaborations have reported[12-14] an enhancement to the Born term by a factor of 2, but with large errors. There has been some speculation that this could be due to a low-mass resonance, but no corresponding signal has been seen[11,5] in the neutral channel.

We report here on a new high-statistics measurement of the cross section for reaction (1) using 209 pb^{-1} of data taken with the Mark II detector at the SLAC storage ring PEP. The cross section for $\gamma\gamma\rightarrow\pi^+\pi^-$ is extracted over the range of pion-pair invariant masses $M(\pi^+\pi^-)$ between 350 MeV/c^2 and 1.6 GeV/c^2 and compared to predictions of several models.[15-17]

II. THE DETECTOR

The Mark II detector and data processing have been described elsewhere.[18] We reiterate here those features of the detector which are important to this analysis.

A. Tracking

Tracking information was provided by the main drift chamber (DC), in conjunction with the vertex chamber (VC). The DC consisted of sixteen concentric layers of sense wires, covering radii between 41 and 145 cm from the beam axis. The position resolution was approximately 200 μm in the xy plane at each layer. Ten of the layers were tilted at an angle of ±3° with respect to the beam (z) axis. The resulting stereo information was used to measure the z position. The VC was a high-resolution drift chamber. It consisted of an inner band of four layers of sense wires at a radius of ~ 10 cm, and an outer band of three layers at a radius of ~ 30 cm. In this experiment the DC and VC were immersed in a 2.3-kG conventional solenoidal magnet, with the field along the z axis. The coil consisted of 1.4 radiation lengths and 0.3 interaction lengths of aluminum at a radius of 1.6 m. The combined information from the DC and the VC provided a momentum resolution in the xy plane of $(\sigma_{p_{xy}}/p_{xy})^2=(0.025)^2+(0.011p_{xy})^2$ (p_{xy} in GeV/c).

B. Time of flight

The time-of-flight (TOF) system consisted of 48 scintillation counters at a radius of 1.51 m, just inside the magnetic coil. Each counter was read out at both ends by phototubes. The rms resolution, averaged over the duration of the run, was 375 psec. This timing, combined with the tracking information, allowed π-μ separation up to momenta of ~ 150 MeV/c, π-e separation up to ~ 200 MeV/c, K-π separation up to ~ 830 MeV/c, and proton identification up to ~ 1.4 GeV/c. It also allowed unambiguous identification of cosmic-ray events.

C. Calorimetry

The liquid-argon calorimeter (LA), consisting of eight modules surrounding the magnet coil at a minimum radius of 1.8 m, provided electromagnetic calorimetry over a solid angle of 64% of 4π. Each module consisted of 37 planes of 2-mm-thick lead and/or antimony spaced 3 mm apart and immersed in liquid argon. Signal planes and ground planes were alternated. The signal planes were divided into strips running in one of three different directions: 3.8-mm strips parallel and perpendicular to the beam to measure azimuth and polar angle, respectively, and 5.4-mm strips at a 45° angle to resolve ambiguities. The front of each module also contained a trigger gap—three 1.6-mm-thick aluminum planes separated by 8 mm of liquid argon. The central plane was the signal plane and was segmented into strips perpendicular to the beam axis. The trigger gap was used to identify and correct the energy of showers that began in the magnet coil. The total calorimeter thickness was 14.5 radiation lengths, and the energy resolution for electromagnetic showers was $\sigma_E/E = 14\%/\sqrt{E}$. Use of the LA to identify pions will be explained in Sec. III.

D. The trigger

Events of interest in this analysis typically satisfied the charged trigger, which required at least two tracks, each with at least six DC and VC hits and one TOF hit. These hits had to lie on one of 24 different predefined roads of curvature, defined in programmable coincidence modules known as curvature modules. The curvature modules were $>98\%$ efficient at finding tracks which were within our fiducial volume, had momenta greater than 400 MeV/c, and originated at the interaction point (IP). A measurement of the charged trigger efficiency is described in Sec. IV B.

III. EVENT SELECTION AND PARTICLE IDENTIFICATION

The most important problem in studying reaction (1) is the elimination of the dominant two-prong QED reactions $e^+e^- \to e^+e^-e^+e^-$ and $e^+e^- \to e^+e^-\mu^+\mu^-$. In Fig. 1 we show predicted cross sections for the two-photon production of pion pairs and lepton pairs. One sees that except near the $f_2(1270)$ resonance, the leptonic backgrounds are much larger than the expected signal.

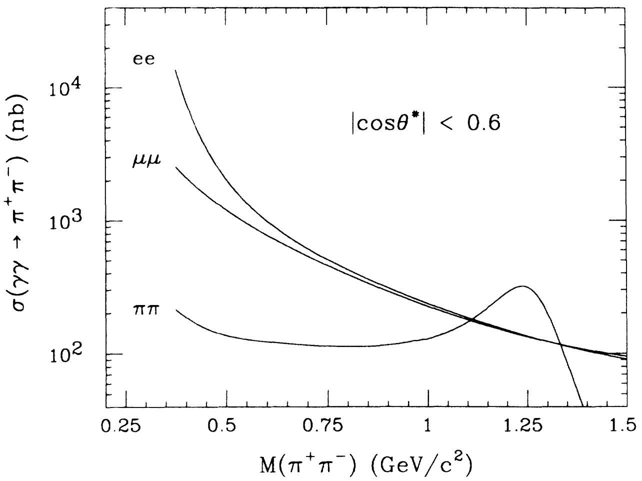

FIG. 1. Predicted two-photon cross sections for pion pairs and lepton pairs. The predictions for lepton pairs are from a Monte Carlo calculation. The prediction for pion pairs is that of Morgan and Pennington (Ref. 15), where the pion-pair cross section consists of a nonresonant continuum and the large $f_2(1270)$ resonance. The observed peak of the $f_2(1270)$ is shifted due to interference with the continuum.

We select two-prong events with net transverse momentum with respect to the e^+e^- axis, $\sum p_t$, less than 150 MeV/c. Both tracks are required to reach the TOF counters and to hit an active region of the LA calorimeter. This selection results in approximately 1.5×10^6 events with $M(\pi^+\pi^-)$ between 350 MeV/c^2 and 1.6 GeV/c^2. Their mass spectrum is shown in Fig. 2. One already sees the $f_2(1270)$ resonance over the leptonic background. To remove the lepton pairs, we then use two different methods of particle identification, depending on the average momenta of the tracks. For $M(\pi^+\pi^-)$ between 350 and 400 MeV/c^2, we identify pion pairs using the TOF system. For $M(\pi^+\pi^-)$ between 540 MeV/c^2 and 1.6 GeV/c^2, we use the LA calorimeter. Between 400 and 540 MeV/c^2, we have no reliable particle identification.

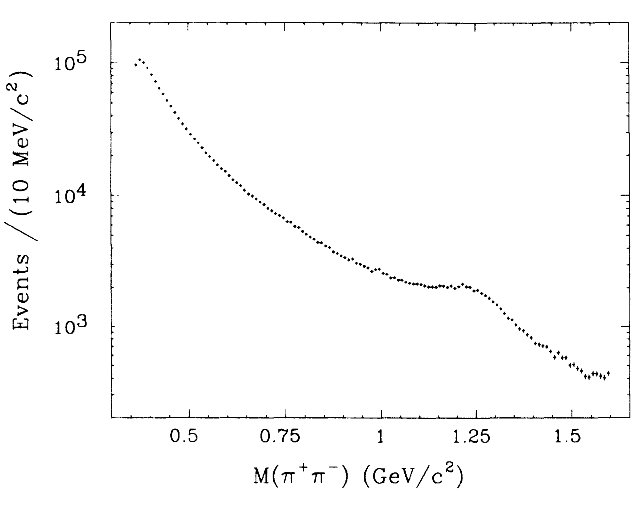

FIG. 2. Invariant-mass spectrum of all accepted two-prong events (calculated with all tracks considered as pions).

A. TOF identification

The effective TOF resolution is somewhat improved for pair events, because each event must have two tracks of the same mass. The difference between $t_{\pi\pi}$ and $t_{\mu\mu}$ (the expected values of $t_{1+2}=t_1+t_2$ for pion pairs and muon pairs, respectively) is twice the difference in expected TOF for an individual track, while the resolution in t_{1+2} is only a factor of $\sqrt{2}$ poorer than the single-track resolution.

In Fig. 3, we plot $t_{1+2}-t_{\pi\pi}$ for events with $t_{\pi\pi}-t_{\mu\mu}$ greater than 2 nsec. The resolution for low-momentum tracks is substantially worse than that measured for Bhabha events, due to the uncertainty in the track's measured momentum and path length to the TOF counters. The resolution for pions is also slightly broadened by decays in flight.

The net result is that the measured resolution $t_{1+2}-t_{\pi\pi}$ is close to 700 psec. Therefore, for TOF separation at about the 3σ level, we require $t_{\pi\pi}-t_{\mu\mu}>2$ nsec. This limits the usefulness of TOF identification to $M(\pi^+\pi^-)$ below 400 MeV/c^2.

B. LA identification

For larger invariant masses, we use a technique that was previously developed for the Mark II at the SLAC storage ring SPEAR.[10] Before entering the LA calorimeter, a particle must traverse 12 cm of aluminum in the 0.3 interaction length magnet coil. Pions will frequently interact in the coil, causing them to scatter outside an extrapolated path through the LA calorimeter. The total energy associated with a track (E_{LA}) is that deposited within a road centered on its extrapolated path. We can identify those pions whose extrapolated paths through the LA calorimeter contain less than a threshold energy. Leptons generally do not scatter through large angles in the coil. Therefore, most of the energy deposited by leptons is included in E_{LA}. Minimum-ionizing muons deposit about 250 MeV, and electrons deposit all their energy. Therefore, by requiring that a charged track of momentum >200 MeV/c has $E_{\mathrm{LA}}<130$ MeV, we select a sample that is enriched in pions. The efficiency for pion identification and the misidentification probabilities for muons and electrons by this method can be independently determined. The self-consistency between cases of one pion identified by this method and two pions so identified provides an additional measure of these probabilities. As will be seen, this method leaves a large event sample of reaction (1) with minimal background at masses above $M(\pi^+\pi^-)=700$ MeV/c^2.

We introduce the following notation: $P_{\mathrm{ID}}(i)$ is the probability that particle i will satisfy the criteria for identification as a pion using the LA calorimeter as described below. Thus $P_{\mathrm{ID}}(\pi)$ is the pion identification probability, while $P_{\mathrm{ID}}(e,\mu)$ are the probabilities that a muon or electron will be misidentified as a pion. $P_1(\pi\pi)$ and $P_2(\pi\pi)$ are the probabilities that one or both pions in a pion-pair event will be correctly identified. Similarly, $P_1(ee,\mu\mu)$ and $P_2(ee,\mu\mu)$ are the probabilities that one or both leptons in a lepton-pair event will be misidentified as pions.

$P_{\mathrm{ID}}(\pi)$ is calibrated using pions from the reaction

$$e^+e^-\to e^+e^-\pi^+\pi^-\pi^+\pi^- \tag{2}$$

identified with a similar $\sum p_t$ criterion. Events containing kaons or protons identified by their TOF have been removed. Events containing e^+e^- pairs from converted photons have also been removed. The remaining sample of calibration pions is estimated to be at least 95% pure. In Fig. 4(a) we show a scatter plot of the track momentum p vs E_{LA}, for pions from this sample. $P_{\mathrm{ID}}(\pi)$ is independently checked using pions reconstructed as coming from the decays of K_S^0 mesons.

$P_{\mathrm{ID}}(e)$ is calibrated using electrons from photon conversions and from low-mass two-prong events where at least one track has been identified as an electron by its TOF. $P_{\mathrm{ID}}(\mu)$ is measured using the copious supply of

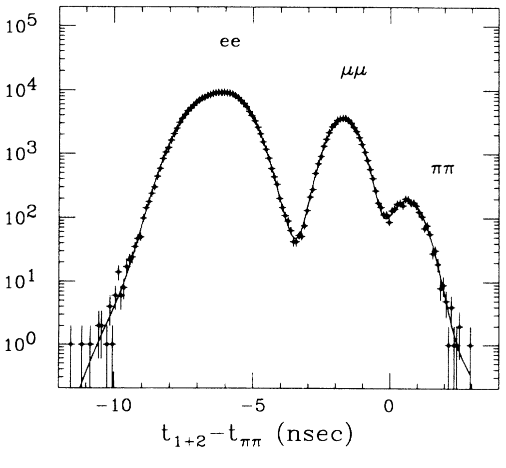

FIG. 3. $t_{1+2}-t_{\pi\pi}$ plotted for all pairs with $M(\pi^+\pi^-)$ between 350 and 400 MeV/c^2 such that $t_{\pi\pi}-t_{\mu\mu}>2$ nsec. The results of a fit to determine the number of pion pairs, electron pairs, and muon pairs are shown.

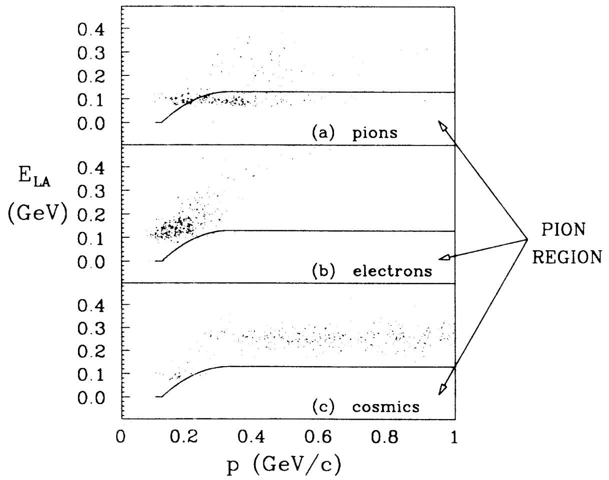

FIG. 4. E_{LA} vs momentum: (a) π's, (b) e's, (c) μ's. Tracks below the solid line are identified as pions.

cosmic-ray events interspersed in the regular data. In Figs. 4(b) and 4(c) we show the same plot for the lepton calibration samples. The solid line shows the energy threshold for pion identification. Tracks below the threshold are called pions. The $P_{\rm ID}(\pi,e,\mu)$ are obtained from these plots and are shown in Fig. 5. However, correlations between the $E_{\rm LA}$ of the two portions of a cosmic-ray track indicate that a sizable fraction of the lower-momentum tracks in this sample are actually secondary pions. Hence the muon misidentification probability measured is really an upper limit. Therefore, $P_{\rm ID}(\mu)$ will be adjusted so that the cross section for reaction (1) is the same whether determined from events with one or two pions identified.

IV. NORMALIZATION

The normalization used to compute the measured cross section is determined from the luminosity and the efficiency and then checked against known lepton pair cross sections. The total luminosity, 209 $\rm pb^{-1}$, for the data used in this analysis is measured using wide-angle Bhabha-scattering events.[19]

Except for certain factors which have not been included in the detector simulation, the efficiency is determined by Monte Carlo simulation. Where they differ, $\mathcal{E}^{\rm LA}$ and $\mathcal{E}^{\rm TOF}$ refer specifically to the LA- and TOF-identified pair analyses. We divide the total efficiency $\mathcal{E}$ into three factors:

$$\mathcal{E}=\mathcal{E}_{\rm MC}\mathcal{E}_{\rm trigger}\mathcal{E}_{\rm DC}\ . \tag{3}$$

We expect these efficiency factors to be nearly the same for the QED processes $\gamma\gamma\to e^+e^-$ and $\gamma\gamma\to\mu^+\mu^-$ as they are for $\gamma\gamma\to\pi^+\pi^-$. In this section we will discuss each of these factors and then use them to measure the known lepton pair cross sections as a check on the overall normalization.

For about half of the data, the drift-chamber voltage was lowered to prevent excessive current draw due to aging wires, causing a loss of efficiency. The resulting efficiency, which we call $\mathcal{E}_{\rm DC}$, was measured[20] by comparing the multiplicity of hadronic events in these runs with that in normal runs. It was thus determined that, independent of momentum, there was an inefficiency of 10% per track in the worst section, decreasing to 2% after oxygen was added to the gas. Using this measurement, we estimate that the observed two-prong efficiency for the 130 $\rm pb^{-1}$ of data which contain the degraded runs is 12% lower than for the normal runs. We have checked the correction for pion-pair masses between 500 $\rm MeV/c^2$ and 1.5 $\rm GeV/c^2$, and find agreement independent of $M(\pi^+\pi^-)$. Applied to the full data sample, the overall correction is $\mathcal{E}_{\rm DC}=0.93\pm0.01$.

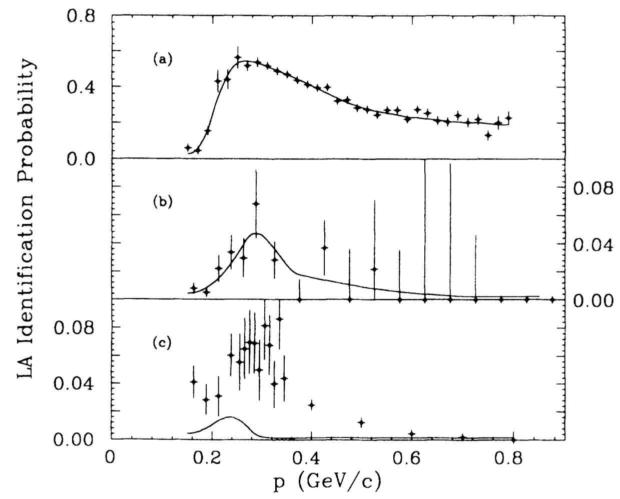

FIG. 5. Probability that $E_{\rm LA}$ is in the "pion region" as defined in Fig. 4 for tracks in the calibration samples: (a) π's, (b) e's, (c) cosmic-ray tracks.

A. Monte Carlo simulation

$\mathcal{E}_{\rm MC}$ is measured using the Monte Carlo event generator called GGDEPA,[21] which is based on the equivalent-photon approximation convoluted either with the lowest-order QED cross section for the production of lepton pairs by real photons or with the Born approximation for pion-pair production. The Low formula used in this generator overestimates the luminosity function by 13–15 % for the $\gamma\gamma$ energies in this analysis, and we simply correct by this factor. The overall normalization of GGDEPA is found to agree (within 2%) with the theoretical lepton-pair cross section[22]

$$\frac{d\sigma}{d\cos\theta^*}=\frac{2\pi\alpha^2}{W_{\gamma\gamma}^2}\frac{\beta(2\beta^2\sin^2\theta^*-\beta^4\sin^4\theta^*+1-\beta^4)}{(1-\beta^2\cos^2\theta^*)^2}\ , \tag{4}$$

where β is the velocity of either lepton in the center of mass, and θ^* is the center-of-mass scattering angle. The $\sum p_t$ distribution for lepton pairs is checked by comparing the visible cross section from GGDEPA with the prediction of a more sophisticated generator, G4QQZO,[23] which calculates the QED cross section for $e^+e^-\to e^+e^-l^+l^-$ directly from all contributing lowest-order diagrams and therefore does not use a luminosity function. (By visible cross section, we mean that both generated tracks are in the fiducial volume defined by the event cuts, and that the $\sum p_t$ is less than 150 MeV/c.) With corrected normalization, GGDEPA agrees with G4QQZO within statistics (2%). Since the $\sum p_t$ distribution for pion pairs could be slightly different, we assign a systematic uncertainty of 5%.

Generated events are then put through the detector simulation. All events are assumed to trigger, so the trigger efficiency must be measured separately. The response of each component of the detector is modeled as closely as possible, including the effects of particle decays, multiple scattering, and electromagnetic interactions. Hadronic interactions are neglected.

$\mathcal{E}_{\rm MC}$ is measured separately for each species as a function of $M(\pi^+\pi^-)$ and $\cos\theta^*$. The resolution of the detector in $\cos\theta^*$ is quite good, and the angular distributions are reasonably well approximated by GGDEPA. Even in a region where the angular distribution is different in the data than it is in GGDEPA [e.g., pion pairs near the $f_2(1270)$ resonance], the cross section is slowly changing relative to the resolution. Therefore, the systematic error in the angular dependence of the efficiency is $\sim 5\%$ for $|\cos\theta^*| > 0.5$ and negligible for small $|\cos\theta^*|$. In fitting to a theoretical model which may have structure that is small relative to the resolution in $M(\pi^+\pi^-)$, we will smear the theoretical prediction by the measured detector resolution before comparing to the data.

B. Trigger efficiency

Low-energy two-photon events generally satisfy only the charged trigger, which requires that at least two tracks be found with one or more curvature modules fired. Firing modules with overlapping roads are combined. The curvature modules also provide an initial estimate of the azimuthal angle of each track, with a resolution of about 5°. In order to measure the probability that a charged track will latch (be found by the hardware), we look at 4-prong events in which two other tracks satisfy the single-track latch criteria. In Fig. 6 we plot the latch efficiency as a function of p_t, the component of the track momentum in the xy plane. One can see that it drops off sharply for $p_t < 100$ MeV/c, and that the errors are fairly large. Therefore, to ensure that the trigger efficiency is well known, we will require that $p_t > 100$ MeV/c.

Except for a very small number of runs, the charged trigger required 2 tracks found by the hardware. Therefore the event trigger efficiency ($\mathcal{E}_{\text{trigger}}$) is the product of the latch efficiencies of the two tracks in the event. Since tracks with different p_t contribute to a given bin of $M(\pi^+\pi^-)$ and $\cos\theta^*$, we use the Monte Carlo simulation to determine $\mathcal{E}_{\text{trigger}}$ from the p_t spectrum and the single-track latch efficiency. This is done by weighting each event from the Monte Carlo simulation, which has passed all the analysis cuts (including the requirement that $p_t > 100$ MeV/c for each track) by the probability that the event triggered. The efficiency for that bin is then the sum of all the event weights divided by the number of events. In the mass region of the LA analysis, the trigger efficiency rises from 95% at 550 MeV/c^2 to its full value of 97% at 700 MeV/c^2 with a systematic uncertainty of about 1%.

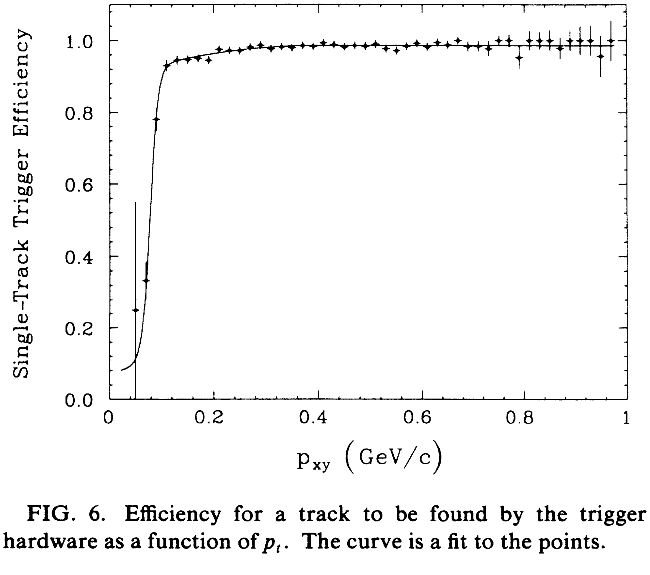

FIG. 6. Efficiency for a track to be found by the trigger hardware as a function of p_t. The curve is a fit to the points.

For $M(\pi^+\pi^-)$ below 400 MeV/c^2, pions are identified by their TOF. Now the minimum p_t cut is lowered to 90 MeV/c, and there is effectively a maximum p_t cut imposed by the requirement that pions can be distinguished from muons by their TOF. This puts us in a region where the trigger efficiency is not as well known, and we assign an uncertainty of 6–10 % to this trigger efficiency. Since the trigger efficiency is measured with pions, we assign an additional systematic uncertainty of 6% to the lepton trigger efficiency.

C. TOF-identified lepton pairs

In this section we present separate measurements of the lepton-pair spectra for $W_{\gamma\gamma} < 360$ MeV, as a check on the normalization.

As previously mentioned, the cuts for TOF-identified pairs are slightly different than for LA-identified pairs. We require that all tracks have $p_t > 90$ MeV/c, that both tracks hit good TOF counters, and that the expected value of t_{1+2} for the lepton pair (t_{ll}) is at least 2 nsec away from the expected value for all other mass hypotheses. We also require that the position at which a track hits the TOF counter, as determined from the difference of the signal times at the two ends of the scintillator, agrees with the value projected from the DC track within 25 cm.

We use a 168 pb^{-1} subsample of the data. To determine the number of electron or muon pairs in a given mass bin, we fit the distributions in $t_{1+2} - t_{ll}$ for all pairs in that bin, such that $t_{\mu\mu} - t_{ee}$ for electron pairs or $t_{\pi\pi} - t_{\mu\mu}$ for muon pairs is at least 2 nsec. Only the peak for the species being measured will be Gaussian. The other peaks will be a sum of Gaussians centered at different distrances from the central peak. (The number of pion pairs will be determined in the same way.) An example of such a plot is shown in Fig. 3. The systematic errors from the fit are less than 5%, which is small compared to other sources of systematic error in this measurement.

The measured cross sections for $\gamma\gamma$ production of x^+x^- pairs as a function of $W_{\gamma\gamma}$ (summed over $\cos\theta^*$ assuming the angular distribution is known) are determined from the detected number N_{xx} of x^+x^- events as follows:

$$\sigma(\gamma\gamma \to x^+x^-) = \frac{dN_{xx}/dW_{\gamma\gamma}}{\mathcal{L}\mathcal{E}_{\text{event}} d\mathcal{L}_{\gamma\gamma}/dW_{\gamma\gamma}} , \tag{5}$$

where $\mathcal{L}$ is the luminosity that $d\mathcal{L}_{\gamma\gamma}/dW_{\gamma\gamma}$ is the luminosity function approximated by the (corrected) Low formula

$$\frac{d\mathcal{L}}{dz} = 4\left[\frac{\alpha}{\pi}\right]^2 \frac{1}{z}\left[\ln\frac{E}{m_e}\right]^2 \times \left[2(1+\tfrac{1}{2}z^2)^2 \ln\frac{1}{z^2} - (1-z^2)(3+z^2)\right] , \tag{6}$$

TABLE I. Corrections and efficiences used in calculating measured cross sections.

Correction to the luminosity function	$d\mathcal{L}_{\gamma\gamma}^{\text{true}}/dW_{\gamma\gamma}=0.877\times d\mathcal{L}_{\gamma\gamma}^{\text{Low}}/dW_{\gamma\gamma}$			
	TOF-identified pair analysis			LA-identified pair analysis
Efficiency factors	$\pi^+\pi^-$	e^+e^-	$\mu^+\mu^-$	$\pi^+\pi^-,e^+e^-,\mu^+\mu^-$
$\mathcal{E}_{\text{MC}}$	0.3–3 %	0.7–7 %	0.4–4 %	10–13 %
$\mathcal{E}_{\text{trigger}}$	69–83 %	62–92 %	60–84 %	94–98 %
$\mathcal{E}_{\text{DC}}$	93%	93%	93%	93%

where z is the scaled two-photon energy ($z=\sqrt{s}/2E$). Corrections and efficiences used in calculating the measured cross sections from Eq. (5) are summarized in Table I.

In Fig. 7 we compare the measured two-photon cross sections for lepton-pair production with the prediction of Eq. (4). The electron pairs fall below the prediction, while the muons are high relative to the prediction, but the errors are fairly large. The errors are mostly due to systematics and are correlated between points, so the overall disagreement with the prediction is not bad. One large contribution to the error is from the uncertainty in the trigger efficiency which we cannot independently measure for electrons and muons. However, one might suppose that muons, which do not decay or radiate, would trigger more efficiently than electrons. Other possible explanations for observed discrepancies in the lepton-pair cross sections arise because the spectrum is falling steeply while the trigger efficiency is rising. When the cross section is not flat, the finite-mass resolution ($\sim 5\%$ at low masses) can cause systematic shifts in the measurement. However, these effects should be fairly small since the slopes in question are only about 10% per 10 MeV/c^2.

D. Combined lepton-pair spectrum

Since the lepton pairs make up the vast majority of the 2-prong cross section, we can measure the combined lepton-pair cross section as a function of $M(\pi^+\pi^-)$ by simply subtracting the estimated small contribution from pion pairs and the even smaller contribution from other final states. For $M(\pi^+\pi^-)$ below 1 GeV/c^2, this pion-pair contribution is expected to be no more than 15%. Therefore the uncertainty in the measurement of the lepton-pair spectrum due to a conservative estimate of 15% uncertainty in the pion spectrum will be at most 2%.

Using the known equivalent luminosity of a Monte Carlo sample of both electrons and muons, corrected for $\mathcal{E}_{\text{trigger}}$ and $\mathcal{E}_{\text{DC}}$, we then predict the total number of leptonic pairs expected in the final data sample. Figure 8 shows the comparison with the total measured two-prong spectrum, from which the contribution from pion pairs (determined later in this paper) has been subtracted. The agreement is striking and is a convincing test of the normalization.

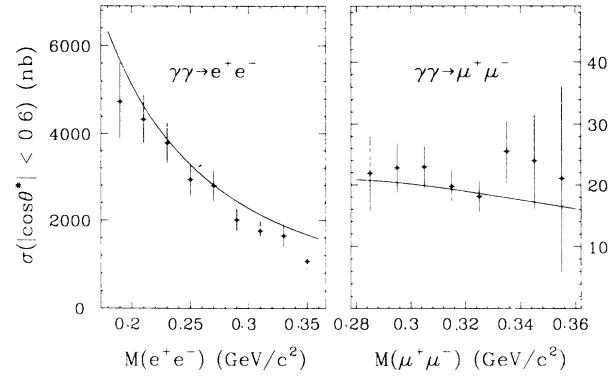

FIG. 7. Fully corrected and normalized measured cross sections for two photon production of lepton pairs, using TOF-identified electrons and muons. The data are compared with the lowest-order QED cross section for the production of lepton pairs by two real photons. The error bars include systematic errors.

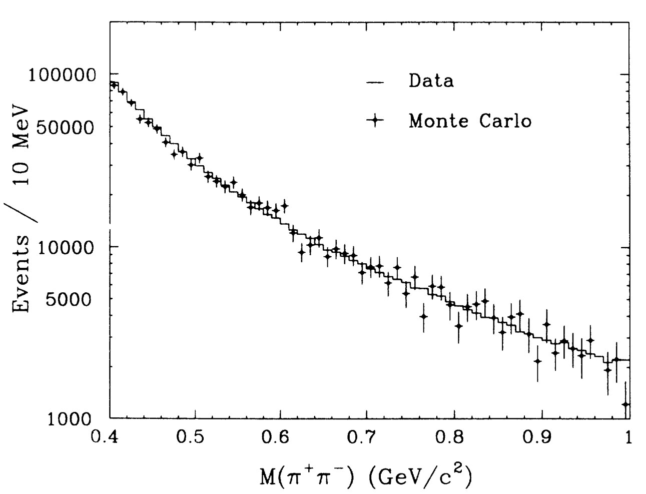

FIG. 8. Number of 2-prong events detected, with the contribution from pion pairs subtracted, compared to a Monte Carlo prediction for electron pairs and muon pairs combined.

V. PION-PAIR SELECTION AND BACKGROUND SUBTRACTION

We now use the particle-identification techniques previously described to extract the pion pairs. Sources of pion pairs other than reaction (1) are then subtracted to obtain the final event sample.

A. TOF-identified pion pairs

The details of TOF identification of pion pairs between 350 and 400 MeV/c^2 and of the systematic uncertainty have already been presented. The method closely parallels that used with the lepton pairs. Since the acceptance is a strongly correlated function of $M(\pi^+\pi^-)$ and $\cos\theta^*$, it is difficult to extract meaningful information about the angular distribution in this low-mass region. We will assume that it is well described by the Born approximation, which is nearly flat for $\cos\theta^* < 0.6$.

Most of the systematic uncertainty in the cross section comes from the measurement of the efficiency and from the overall normalization, and not from the fit to $N_{\pi\pi}$. In Fig. 9, we show the cross section from TOF-identified pion pairs. The error bars include all systematic errors except for the overall normalization. The data are compared to the Born approximation and to the fit of Morgan and Pennington.[15] Our results agree quite well. Other experiments[12–14] have reported an enhancement by a factor of two relative to the Born term in this mass region, with large uncertainties. Our data covers the mass range between 350 and 400 MeV/c^2, which corresponds to one point from each of these experiments, and does not confirm such an enhancement.

B. LA-identified pion pairs

We separately analyze events with one and two pions identified in the LA. The leptonic backgrounds are subtracted, and then the pion-pair spectra are corrected by the measured probabilities to identify one or two pions. We then check that the two resulting distributions agree. Where they do, we have obtained a more reliable measurement of the pion-pair cross section than would be possible using only one sample. Where they differ, we force agreement by allowing for corrections to $P_{\rm ID}(\pi,e,\mu)$ consistent with the measured values.

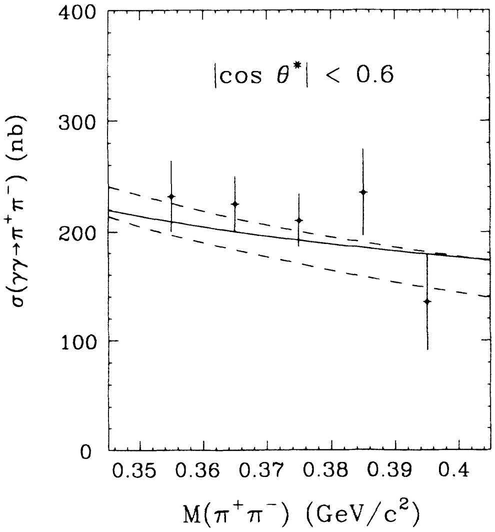

FIG. 9. Pion-pair cross section from TOF-identified pion pairs. The solid curve is the Born approximation. The dashed curves show the range of allowed values of the Born term plus final-state interactions in the model of Morgan and Pennington.

We use the measured single-track probabilities $[P_{\rm ID}(\pi,e,\mu)]$ to determine the pair probabilities $[P_n(\pi\pi,ee,\mu\mu)]$, that a given number of tracks in each event type will be identified as a pion, as a function of $M(\pi^+\pi^-)$ and $\cos\theta^*$ as follows:

$$P_1(\pi\pi)=P_{\rm ID}(\pi_1)[1-P_{\rm ID}(\pi_2)]+P_{\rm ID}(\pi_2)[1-P_{\rm ID}(\pi_1)] \qquad (7)$$
$$P_2(\pi\pi)=P_{\rm ID}(\pi_1)P_{\rm ID}(\pi_2)\ .$$

The $P_n(ee,\mu\mu)$ are determined similarly. The pair probabilities $P_n(\pi\pi,ee,\mu\mu)$ are then averaged over all detected events contributing to each bin of $M(\pi^+\pi^-)$ and $\cos\theta^*$.

We must also estimate the uncertainty associated with $P_n(\pi\pi,ee,\mu\mu)$. Since the averaging process itself is performed over many events, only negligible uncertainty is introduced. The uncertainty in $P_{\rm ID}(\pi)$ is known from the fit. For events where both tracks have the same values of p and LA entry point $(z_{\rm LA})$, the uncertainty on the identification probability of the two tracks is completely correlated:

$$\delta P_2(\pi\pi)=2P_{\rm ID}(\pi)\delta P_{\rm ID}(\pi)\ . \qquad (8)$$

However, when p and $z_{\rm LA}$ of the tracks are different, the uncertainties are only partially correlated. For partially correlated errors with a correlation coefficient C, we may write the uncertainty in $P_n(\pi\pi)$ as

$$\delta^2P_n(\pi\pi)=\partial_iP_n(\pi\pi)V_{ij}\partial_jP_n(\pi\pi)\ , \qquad (9)$$

where V is the error matrix:

$$V=\begin{bmatrix} \delta^2P_{\rm ID}(\pi_1) & C\delta P_{\rm ID}(\pi_1)\delta P_{\rm ID}(\pi_2) \\ C\delta P_{\rm ID}(\pi_1)\delta P_{\rm ID}(\pi_2) & \delta^2P_{\rm ID}(\pi_2) \end{bmatrix}\ . \qquad (10)$$

We estimate the correlation coefficient by altering the measured pion identification probability for each momentum bin and refitting. We may describe the change as a Gaussian of width σ_p in momentum space and write the correlation coefficient as

$$C=\exp\left[\frac{-(p_1-p_2)^2}{2\sigma_p^2}\right]\ . \qquad (11)$$

The uncertainty in $P_n(\pi\pi,ee,\mu\mu)$ is then averaged over all events in each bin of $M(\pi^+\pi^-)$ and $\cos\theta^*$.

The next step is to use the measured values of $P_n(\pi\pi,ee,\mu\mu)$ to determine the leptonic background and correct for the identification efficiency. We use the Monte Carlo simulation to tell us the relative population of electrons and muons in the detected sample. The lepton-pair misidentification probability $[P_n(ll)]$ is then the average of $P_n(ee,\mu\mu)$ weighted by the relative populations. We define N as the total number of events in a given bin (any number observed, including zero) and $N_{\pi\pi}$ as the number of these events that are actually pion pairs. The leptonic background N_n^L in the sample with n identified pions is then

$$N_n^L=(N-N_{\pi\pi})P_n(ll) \ . \tag{12}$$

The detected numbers of events N_n in the samples with n identified pions will be

$$N_n=N_n^L+N_{\pi\pi}P_n(\pi\pi) \ . \tag{13}$$

We may then solve Eqs. (12) and (13) for $N_{\pi\pi}$ in terms of the measured efficiencies $P_n(\pi\pi,ee,\mu\mu)$ and the detected numbers of events N_n:

$$N_{\pi\pi}=\frac{N_n-NP_n(ll)}{P_n(\pi\pi)-P_n(ll)} \ . \tag{14}$$

This gives us independent measurements of $N_{\pi\pi}$ from the event samples with 1 and 2 pions identified, respectively. If $P_n(\pi\pi,ee,\mu\mu)$ have been well measured, the two independent values of $N_{\pi\pi}$ will agree. In Figs. 10(a) and 10(b) we show $N_{\pi\pi}$ calculated from Eq. (14) as a function of $M(\pi^+\pi^-)$ for the two samples. In Fig. 10(c), we see from the ratio that the distributions agree quite well for $M(\pi^+\pi^-)>750$ MeV/c^2, but at low masses, where the leptonic background is largest, they do not agree. Therefore, for $M(\pi^+\pi^-)$ greater than 750 MeV/c^2, we may naively combine the samples and use the nominal values of $P_n(\pi\pi,ee,\mu\mu)$. For $M(\pi^+\pi^-)$ below 750 MeV/c^2, we must take a different approach.

We decided instead to fit for $N_{\pi\pi}$, allowing for corrections to $P_n(\pi\pi,ee,\mu\mu)$. To do this, we form a joint χ^2 between the expected and detected numbers of events, N_1 and N_2, and between the measured and corrected values of $P_n(\pi\pi,ee,\mu\mu)$. The fit values of $N_{\pi\pi}$ depend crucially on $P_2(\pi\pi)$. For $M(\pi^+\pi^-)$ below 540 MeV/c^2, $P_2(\pi\pi)$ drops rapidly, and the relative uncertainty rises rapidly from just over 10% at $M(\pi^+\pi^-)=540$ MeV/c^2 to near 50% at 450 MeV/c^2. We conclude that this method is only good for $M(\pi^+\pi^-)>540$ MeV/c^2. For lower $M(\pi^+\pi^-)$, the LA identification method breaks down.

The uncertainty in $P_{\rm ID}(e,\mu)$ from the unknown makeup of the cosmic-ray sample must be estimated. The results of the fit do not depend strongly on this estimate as long as the estimated uncertainties in $P_n(ll)$ are large compared to the uncertainties in $P_n(\pi\pi)$.

Before fitting, we sum over $\cos\theta^*$ and over several bins of $M(\pi^+\pi^-)$ to gain enough statistics to constrain $P_n(\pi\pi,ee,\mu\mu)$. We assume that any correction to $P_n(ll)$ is applied equally to electron pairs and muon pairs. Requiring that the correction be applied only to muon pairs changes the answer very little.

As a check on $P_{\rm ID}(\pi,e,\mu)$, we compare the corrected and measured identification probabilities. They agree very well above 750 MeV/c^2 but diverge at lower masses, confirming our decision to use only the fit values of $N_{\pi\pi}$ at lower masses. The fits yield a measurement of $N_{\pi\pi}$ with errors which include the contribution from uncertainties in $P_n(\pi\pi,ee,\mu\mu)$. They are highly correlated but do give an indication of the systematic uncertainty due to particle identification. After subtracting the leptonic background contributions, we must still consider sources of pion pairs from processes other than $\gamma\gamma\to\pi^+\pi^-$.

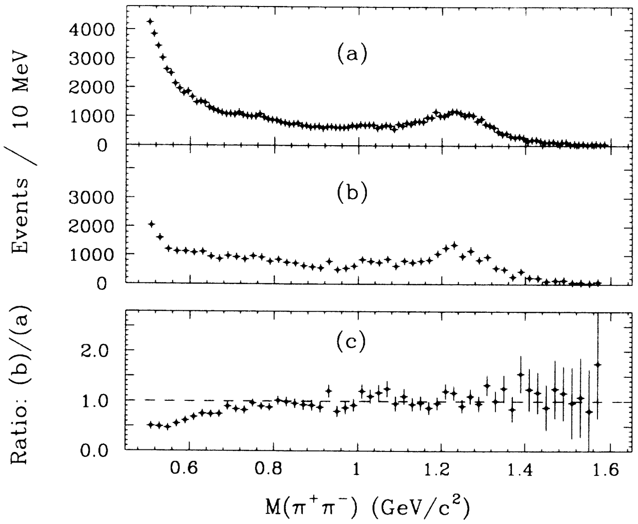

FIG. 10. Pion-pair spectra with leptonic background subtracted, corrected for pion identification efficiency based on the LA method [Eq. (14)], for samples with (a) 1 track identified as a pion, and (b) both tracks identified. The normalization gives the total number of detected (but not necessarily identified) pion-pair events. In (c), we show the ratio of (b)/(a). The expected value, 1.0, is shown as a dashed line.

C. Beam-gas background

Since beam-gas events are distributed nearly uniformly along the beam line, this background can be estimated by looking at events with primary vertex $|z_V|$ greater than 5 cm. In Fig. 11, we plot z_V for events passing all cuts except the z_V cut. One can see a large peak at $|z_V|<5$ cm over a fairly flat continuum.

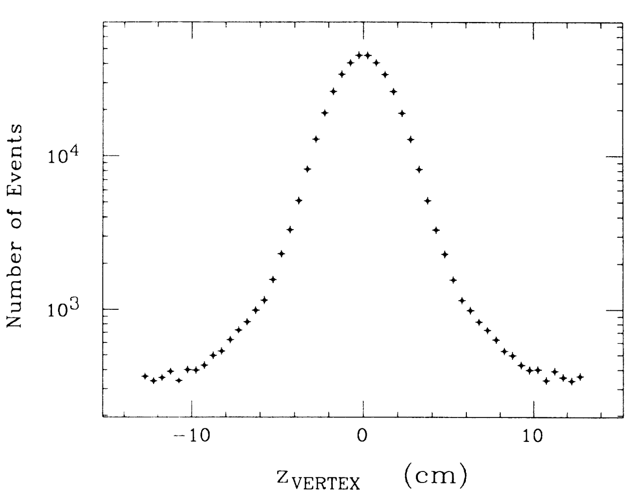

FIG. 11. Vertex position along the beam axis for events passing all cuts except for the z_V cut.

The situation is somewhat complicated by the fact that some real events (i.e., e^+e^- interactions) are reconstructed with $|z_V| > 5$ cm. This is due both to non-Gaussian tails on the beam spot, which has a nominal resolution in z of 1.5 cm, and to hard scattering in the beam pipe, causing the reconstructed vertex position to be displaced. Neither of these effects are well simulated by the Monte Carlo program. Our method for disentangling the beam-gas contribution is to look at the $\sum p_t$ distribution. Beam-gas events have a broad distribution in $\sum p_t$. In Fig. 12, we plot the $\sum p_t$ distribution for three different bins of z_V. The shape of the $\sum p_t$ distribution for beam-gas events is determined from events with $|z_V| > 10$ cm. The normalization of beam-gas events for $|z_V|$ between 5 and 10 cm is allowed to float. Normally, one would expect that the normalization would be the same, but some events with $|z_V| > 10$ cm were lost because of a cut on the data summary tapes which required at least one track to be within 10 cm of the interaction point. We do however expect that the beam-gas normalization will be flat for $|z_V| < 10$ cm.

To determine the mass dependence of the beam-gas background, we use the shape of the $\sum p_t$ distribution above together with the shape of the $\sum p_t$ distribution of the real events from Fig. 12(a). In Fig. 13(a) we plot the expected number of beam-gas events in the full data sample. The $\cos\theta^*$ dependence of the beam-gas background is found to be isotropic.

We must also determine the composition of the beam-gas background. To do this, we fit the data for 5 cm $< |z_V| < 10$ cm to determine the contributions from pion pairs and lepton pairs. We follow the procedure described earlier for the data, using the observed numbers of events with 0, 1, or 2 tracks identified as pions to fit the pion-pair contribution. We find that the fit pion-pair spectrum is in agreement with the hypothesis that beam-gas events are all pion pairs. Therefore, we will subtract the unidentified beam-gas spectrum plotted in Fig. 13(a) from the identification efficiency corrected pion-pair spectrum. This background is about 10% at 550 MeV, dropping rapidly to less than 1% at 1 GeV.

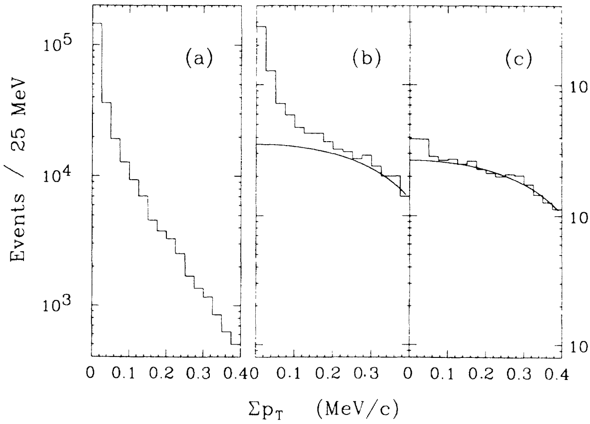

FIG. 12. $\sum p_t$ distributions for events with (a) $|z_V| < 5$ cm, (b) $5 < |z_V| < 10$ cm, and (c) $10 < |z_V| < 15$ cm. The curves in (b) and (c) are fits to the contribution from beam-gas events. Only 30 pb^{-1} of data is shown.

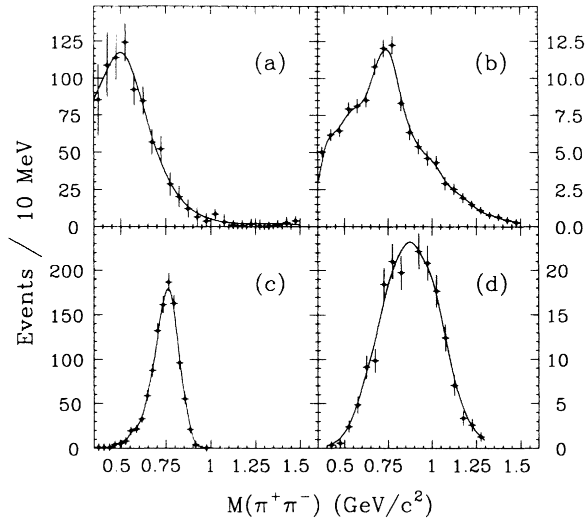

FIG. 13. Invariant pion pair mass distributions of hadronic backgrounds: (a) beam-gas data; (b) $\rho^0\rho^0 \to \pi^+\pi^-\pi^+\pi^-$ (data) $+\rho^+\rho^- \to \pi^+\pi^-\pi^0\pi^0$ (Monte Carlo data); (c) $\eta' \to \rho^0\gamma$ (Monte Carlo data); (d) $a_2(1320) \to \rho\pi$ (Monte Carlo data). The normalization is the same as in Fig. 10.

The beam-gas background for TOF-identified pion pairs is found by the same method to be about 1%.

One byproduct of this method is that we determine the inefficiency due to the z_V cut. It is about 2%, compared to the Monte Carlo prediction of 1.3%, and we correct for this slight difference.

D. Background from four prongs

The two-photon production of four pions is quite large and is dominated by the channel $\gamma\gamma \to \rho\rho \to \pi\pi\pi\pi$. This is a background to pion pairs in the case where two pions are missed down the beam pipe, or where two of the pions are neutral. To estimate this background we determine the mass spectrum of the background by looking at all oppositely charged pairs embedded in 4-prong events. Each pair must satisfy the 2-prong events cuts. We then use a Monte Carlo simulation to normalize the background. To simulate the 4-prong continuum, we create a broad resonance at 1.6 GeV with width 0.5 GeV which we force to decay into $\rho^0\rho^0$. We then take the ratio of 2-prong events from this sample, which pass our acceptance criteria, to pairs embedded in 4-prong events from the same sample. This ratio normalizes the $\pi^+\pi^-\pi^+\pi^-$ background. Although the normalization varies by 50% depending on the angular distribution assumed in the Monte Carlo simulation, the actual background is less than 2% at the ρ peak and less than 1% everywhere else.

The cross section for $\gamma\gamma \to \rho^+\rho^-$ is lower than for $\rho^0\rho^0$, but the efficiency is slightly higher because the neutral pions may go anywhere. This background is approximately 1% at 850 MeV/c^2. The combined contributions from $\rho^+\rho^-$ and $\rho^0\rho^0$ are shown in Fig. 13(b).

E. Background from the η'

We must also consider the background from two-photon production of resonances which decay into pion pairs and other neutral particles. The largest of these is the η', and its dominant 2-prong decay modes are $\eta' \to \rho^0\gamma$ and $\eta' \to \eta\pi^+\pi^-$. From Monte Carlo studies we find that the $\eta\pi^+\pi^-$ background is negligible above 500 MeV/c^2 and amounts to approximately 5% of the TOF identified pions. The $\rho^0\gamma$ background is the largest single background and amounts to 20% of the data at the ρ peak. We show the expected background in Fig. 13(c). The uncertainty on the background is approximately 20% and is dominated by the uncertainties in the Monte Carlo $\sum p_t$ distribution and in the radiative width of the η'.

F. Background from the $a_2(1320)$

The only other resonance with a large two-photon width which decays into two pions plus neutrals is the $a_2(1320)$, which decays predominantly into $\rho^+\pi^-$ (or the charge conjugate). The neutral decay $[a_2(1320) \to \rho^0\pi^0]$ is forbidden. The expected background from the $a_2(1320)$, as determined by Monte Carlo simulation, is shown in Fig. 13(d). It amounts to approximately 3% of the data at 850 MeV/c^2.

The fit pion spectrum is shown rebinned in Fig. 14, with all known hadronic backgrounds subtracted. The subtracted background is shown by the solid curve.

G. Other backgrounds

Kaon and proton pairs are rejected efficiently by the TOF cut, and their cross sections are relatively small compared to the pion-pair cross section (primarily because the actual kaon- or proton-pair mass is much larger than the calculated pion pair mass, and the $\gamma\gamma$ luminosity is correspondingly reduced). Both backgrounds are estimated to be less than 0.1%. Other backgrounds checked with the Monte Carlo simulation and found to be negligible include hadronic annihilation events and τ pairs (both annihilation and two-photon produced).

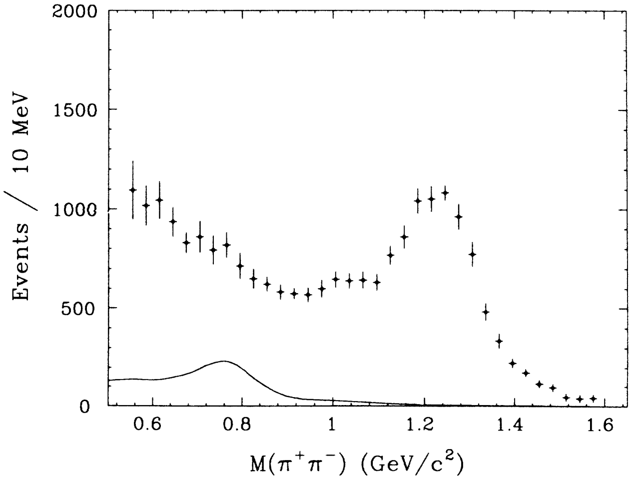

FIG. 14. Pion-pair spectrum from joint fit to identification efficiencies and the distributions with 1 and 2 identified pions. The errors include the systematic errors from the identification. The normalization is the same as in Fig. 10. The curve corresponds to the subtracted background.

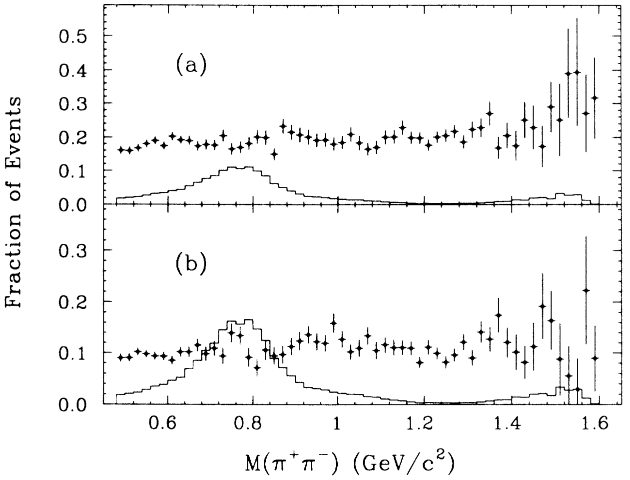

FIG. 15. Fraction of pion-pair event sample with (a) $50 < \sum p_t < 100$ MeV/c, and (b) $100 < \sum p_t < 150$ MeV/c. The histogram is the ratio of the subtracted hadronic backgrounds (see Fig. 13) in each $\sum p_t$ range to the total number of pion pairs shown in Fig. 14.

Backgrounds consisting of two pions plus other particles will have a very different $\sum p_t$ distribution than exclusive pion pairs. For example, 55% of the η' background has pion pair $\sum p_t$ between 100 and 150 MeV/c, as compared to only 10% of the data. By looking at the $\sum p_t$ distribution as a function of invariant mass, we can place a limit on other such backgrounds to the extent that they have noticeable mass structure. We can also check the reasonableness of the backgrounds we have already subtracted. We consider all events with at least one identified pion. Using the measured pion identification probabilities, we can predict the contribution to this sample from the known backgrounds. In Fig. 15, we plot the fraction of the event sample in the $\sum p_t$ ranges 50 to 100 MeV/c and 100 to 150 MeV/c. The histogram is the normalized background which has already been subtracted. One can see that the contribution from the ρ background is quite evident in both $\sum p_t$ ranges. There appears to be some remaining structure, but it is not correlated between Fig. 15(a) and Fig. 15(b). Any background which, like the ρ, is peaked at high $\sum p_t$, as is expected if there are missing particles, should be visible if it is as large as 10% of the data. We conclude that there is no other such background.

VI. ANALYSIS AND RESULTS

We fit the measured cross section to a comparatively simple phenomenological model and also compare our data to the predictions of some more complex models. Our simple model may violate constraints imposed by theory, some of which are satisfied by more complex models, but we will discuss the sensitivity of the measured radiative widths to these constraints. In our simple model, we describe the nonresonant continuum in the Born approximation. Any bumps are assumed to be resonances which we parametrize as relativistic Breit-Wigner forms.

A. The Born approximation

The Born approximation, which assumes a pointlike coupling of the photons to charged spin-zero mesons, gives[24]

$$\frac{d\sigma(\gamma\gamma\to\pi^+\pi^-)}{d\cos\theta^*}=|\mathcal{B}_0|^2+|\mathcal{B}_2|^2\,,$$
$$\mathcal{B}_0=\frac{\alpha\sqrt{\beta}}{W_{\gamma\gamma}\sqrt{2}}\,\frac{1-\beta^2}{1-\beta^2\cos^2\theta^*}\,, \tag{15}$$
$$\mathcal{B}_2=\frac{\alpha\sqrt{\beta}}{W_{\gamma\gamma}\sqrt{2}}\,\frac{\beta^2\sin^2\theta^*}{1-\beta^2\cos^2\theta^*}\,,$$

where $\mathcal{B}_2$ and $\mathcal{B}_0$ are the helicity-2 and helicity-0 components (referring to the cases where the spins of the photons are parallel and antiparallel, respectively), evaluated at $\gamma\gamma$ invariant mass $W_{\gamma\gamma}$. This approximation should be valid where final-state interactions are negligible, and where the wavelength of the photon is large compared to the size of the pion. Although these conditions hold rigorously[25] only up to the vicinity of the ρ mass, previous experiments[1-12] have indicated that the approximation is reasonable up to the mass of the $f_2(1270)$. The Born approximation has a $1/s$ dependence, while at high masses the cross section has a $1/s^3$ dependence, due to the additional $1/s$ dependence of each pion form factor. In fitting the data, we allow for the possibility that the continuum has an intermediate s dependence.

B. Final-state interactions and unitarity

Unitarity applied to $\gamma\gamma\to\pi^+\pi^-$ leads to an important constraint on the amplitude. The constraint may be written as

$$\mathrm{Im}\mathcal{F}(\gamma\gamma\to\pi^+\pi^-)=\left[\frac{s-4m_\pi^2}{s}\right]^{1/2}\times\sum_n\mathcal{F}^*(\gamma\gamma\to n)\mathcal{T}(n\to\pi^+\pi^-)\,, \tag{16}$$

where $\mathcal{F}$ and $\mathcal{T}$ are scattering matrix amplitudes of definite spin J and isospin I, and the condition holds separately for all J and I. This reduces to the requirement (Watson's theorem)[26] that for every partial wave of definite spin and isospin, the phase of $\mathcal{F}(\gamma\gamma\to\pi^+\pi^-)$ must be the same as the phase of $\mathcal{T}(\pi^+\pi^-\to\pi^+\pi^-)$. [If intermediate states are allowed, the theorem still holds approximately as long as the contribution from other channels is small compared to $\pi^+\pi^-$. For $M(\pi^+\pi^-)$ above the threshold for K^+K^- production, the first other strongly interacting intermediate state, the phase of $\mathcal{F}$ is still constrained, but now in terms of the two amplitudes: $\mathcal{T}(\pi^+\pi^-\to\pi^+\pi^-)$ and $\mathcal{T}(K^+K^-\to\pi^+\pi^-)$.]

Equation (16) is linear in $\mathcal{F}$, so it does not directly constrain the modulus. However, since the amplitude must be unitary, the modulus is constrained in terms of an integral of the phase.

Morgan and Pennington have done exactly this in Ref. 15. They use the measured $\pi^+\pi^-$ phases from hadronic scattering data, and find that the Born term is enhanced near threshold [$M(\pi^+\pi^-)<350$ MeV/c^2] by about 20% with an uncertainty of 10%. They also find that the Born term is suppressed for $M(\pi^+\pi^-)>400$ MeV/c^2 by a similar amount. The effect of the final-state interactions is that in the vicinity of a resonance, pion pairs produced via the real Born amplitude resonate in the final state and acquire the phase of the Breit-Wigner resonance. In this picture, it is not very meaningful to separate the complete amplitude into a resonant and a nonresonant component. One must therefore be very careful to define what is meant by the radiative width when it is measured in the presence of a continuum with the same quantum numbers.

In the case of $\gamma\gamma\to\pi^+\pi^-$, the dominant resonance is the spin-2 $f_2(1270)$. It is believed that the $f_2(1270)$ is produced mostly with helicity 2. Our data support this, as we will show later. In the region of the $f_2(1270)$, the largest component of the Born term is $\mathcal{B}_2$, also helicity 2, so in the simplest nonunitarized model, the Breit-Wigner resonance interferes with $\mathcal{B}_2$. Since we measure the cross section as a function of $\cos\theta^*$ but use unpolarized e^+e^- beams, the interference between terms of different helicity is zero, but we must include the effect of interference between all terms of the same helicity, even if they have different spin.

In a slightly improved version of the most naive model, where we still wish to preserve the illusion that the cross section can be separated into resonant and nonresonant components, we must satisfy Watson's theorem. The phase of the combined amplitude must have the phase of the Breit-Wigner form, whose parameters have been determined in hadronic scattering experiments. Since the cross section is mostly $I=0$, $J=2$, $\lambda=2$, we unitarize this partial wave. To separate out the $I=0$, $J=2$ component of $\mathcal{B}_2$, we write it as a linear combination of spherical harmonics $Y_{J\lambda}$, multiply by Y_{22}, and integrate. The result is

$$\mathcal{B}_{22}=\frac{15\alpha\sqrt{\beta}\sin^2\theta^*}{16W_{\gamma\gamma}\sqrt{2}}\left[\frac{(1-\beta^2)^2}{\beta^3}\ln\frac{1+\beta}{1-\beta}-\frac{2}{\beta^2}+\frac{10}{3}\right]. \tag{17}$$

Now to apply Watson's theorem we must modify the phase of either $\mathcal{B}_{22}$ or the Breit-Wigner amplitude. Guided by Morgan and Pennington,[15] the correct procedure leads to a modified Born term which disappears at the $f_2(1270)$, guaranteeing that the phase is purely imaginary. Mennessier[16] comes to the same conclusion via a similar procedure. The effect on the radiative width of the $f_2(1270)$ is that it must be larger than in the simplest model to explain the observed height of the peak.

A different approach is suggested by Lyth.[17] It is somewhat less aesthetically pleasing but is much easier to implement, and it leads to very similar predictions for the radiative width of the $f_2(1270)$. Lyth allows the coupling for $\gamma\gamma\to f_2(1270)$ to acquire a phase such that at resonance, the Breit-Wigner amplitude has a real part which precisely cancels the Born term. [Aside from the unpleasant aspects of having a complex coupling, this scheme does not guarantee that the phase is correct everywhere. In fact, if one insists that the Born term not be modified, the only way to satisy Watson's theorem is to modify the $f_2(1270)$ amplitude in such a way that the additional piece exactly cancels the Born term everywhere. This would lead to the conclusion that the cross section is completely resonant, which is unrealistic: the phase of the spin-2 partial wave is nonzero even below K^+K^- threshold, where we believe that Watson's theorem must be nearly exact, but the cross section is far higher than can be explained by a Breit-Wigner amplitude alone. Despite these difficulties, we find the Lyth scheme to be a convenient way to estimate the effects of unitarity on the radiative width of the $f_2(1270)$.] This amounts to adding a constant δ_B to the usual phase for the $f_2(1270)$ such that at the mass of the $f_2(1270)$, its amplitude will have a real component (proportional to $\sin\delta_B$) that exactly cancels $\mathcal{B}_{22}$.

C. Parametrization of Breit-Wigner resonances

The mass dependence of a resonance R is given by the relativistic Breit-Wigner expression

$$\mathcal{G}(W)=\frac{8\pi(2J+1)}{W}\times\frac{M_R\Gamma^2(W)B(R\to\gamma\gamma)B(R\to\pi^+\pi^-)}{(W^2-M_R^2)^2+M_R^2\Gamma^2(W)}\ . \tag{18}$$

The angular dependence of a spin-J, helicity-λ resonance is contained in the spherical harmonic $Y_{J\lambda}$. For spin-zero resonances, the full width $\Gamma(W)$ is a constant. However, for higher spin resonances, $\Gamma(W)$ contains an additional mass dependence due to the centrifugal potential which we parametrize[27] as

$$\Gamma(W)=\Gamma_R\left[\frac{q(W^2)}{q(M_R^2)}\right]^{2J+1}\frac{D_J(q(W^2)r)}{D_J(q(M_R^2)r)}\ , \tag{19}$$

where

$$q(s)=\left[\frac{s}{4}-m_\pi^2\right]^{1/2}\ , \tag{20}$$

and where r is an effective interaction radius. For the $f_2(1270)$, r is constrained from hadronic scattering data:[28] $r=5.3\pm1.2\ (\text{GeV}/c)^{-1}$. For tensor resonances, D_J is given by

$$D_2(z)=\frac{1}{9+3z^2+z^4}\ . \tag{21}$$

The branching ratios into $\pi^+\pi^-$ are taken from the Particle Data Group compilation:[29]

$$\begin{aligned}B(f_2(1270)\to\pi^+\pi^-)&=\tfrac{2}{3}\times0.86\ ,\\ B(f_0(975)\to\pi^+\pi^-)&=\tfrac{2}{3}\times0.78\ .\end{aligned} \tag{22}$$

The factor of $\frac{2}{3}$ is the Clebsch-Gordan coefficient for an $I=0$ resonance to decay into $\pi^+\pi^-$ instead of $\pi^0\pi^0$. The phase δ_R of a resonance is given by

$$\tan\delta_R(W)=\frac{M_R\Gamma(W)}{M_R^2-W^2}\ . \tag{23}$$

This still leaves a phase ambiguity which is irrelevant in the absence of any interfering amplitudes. If there is interference, then the observed peak of the cross section will be shifted, and the direction of this shift will resolve the ambiguity. In the case of the $f_2(1270)$ in the $\gamma\gamma\to\pi^+\pi^-$ channel, the interference with the real continuum causes the resonance to be shifted down relative to the known mass. This leads us to assign the phase $\delta_{f_2(1270)}=\pi/2$.

In addition to the $f_2(1270)$, we observe a structure just above 1 GeV/c^2. The only known resonance which decays into a $\pi^+\pi^-$, has mass near 1 GeV/c^2, and has quantum numbers such that it can be produced in $\gamma\gamma$ interactions is the $f_0(975)$. Therefore we will add the $f_0(975)$ to our fit. There could be some scalar continuum that causes the observed shift in this channel, but it would have to be substantially larger than the known scalar component of the Born term, even after modification by final-state-interaction effects. [There has been some speculation that the gradual rise below the $f_0(975)$ could be due to a broad σ resonance[15] with mass in the vicinity of 900 MeV/c^2, and width around 600 MeV. This is just a convenient way to fit the observed phase shift. Since we do not constrain the Born term exactly, and since the angular distribution of $\mathcal{B}_2$ is nearly the same as that of a scalar resonance, we are not sensitive to the existence of such a broad low-mass object in the channel $\gamma\gamma\to\pi^+\pi^-$.] It will turn out that our data is well described by the Born term plus the $f_2(1270)$ plus a scalar resonance [possibly the $f_0(975)$] at a mass of around 1010 MeV/c^2. For convenience, we refer to it as the $f_0(975)$.

D. Fit of the $\pi^+\pi^-$ spectrum

We fit the combined 1-identified and 2-identified data samples for $M(\pi^+\pi^-)$ greater than 750 MeV/c^2, together with the fit $\pi^+\pi^-$ data for $M(\pi^+\pi^-)$ between 540 and 750 MeV/c^2 (Fig. 14) and the TOF-identified data (Fig. 9). We first modify the Born term so as to agree with the fit of Morgan and Pennington, modifying both helicity components in the same way:

$$\begin{aligned}\mathcal{B}'_\lambda&=A_B(s)\mathcal{B}_\lambda\ ,\\ A_B(s)&=A_0+A_1/s\ ,\end{aligned} \tag{24}$$

where $A_B(s)$ is a convenient parametrization of the correction. We reproduce Morgan and Pennington's prediction within their quoted uncertainty for $A_0=0.57$ and

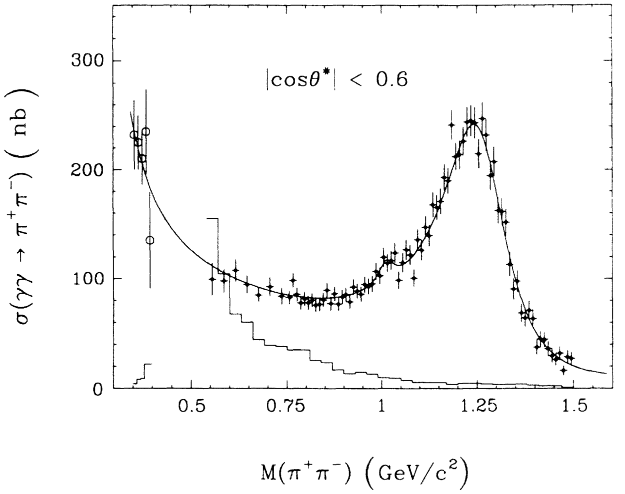

FIG. 16. Results of the fit to the $\pi^+\pi^-$ spectrum. The large circles are the TOF identified data. The other points are the sum of the 1-identified and 2-identified samples in the LA-identified data. The histogram is the subtracted leptonic and hadronic background.

$A_1=0.07$. We can fit most of our data reasonably well using $\mathcal{B}'_\lambda$ only if the mass of the $f_2(1270)$ is allowed to float. Therefore, we allow an additional modification to the Born term:

$$\mathcal{B}''_\lambda = A'_B(s)\mathcal{B}'_\lambda\ , \qquad A'_B(s) = A'_0 + A'_1\sqrt{s} + A'_2 s\ , \tag{25}$$

where A'_B is a parametrization to be determined in the fit.

The results of the fit are shown in Fig. 16. Parameters used in the best fit are listed in Table II, and the data are shown in Table III. In Fig. 17, we compare $\mathcal{B}''_\lambda$ with $\mathcal{B}'_\lambda$ and the nominal Born term. The additional modification we made ($\mathcal{B}''_\lambda$) is slight except at high masses, where one might expect that the continuum would begin to fall off more rapidly because of the onset of a $1/s^3$ mass dependence.[30]

In the above fit, we have used Lyth's method for satisfying Watson's theorem. If we do not unitarize at all, the only appreciable effect on the parameters is that $\Gamma(f_2(1270)\to\gamma\gamma)$ decreases by ~13%.

TABLE II. Parameters of the fit in Fig. 16. The errors are statistical only.

Parameter	Value	Uncertainty
A'_0	0.86	0.18
A'_1	0.62	0.40
A'_2	−0.68	0.21
$\Gamma_{f_2(1270)}$	202 MeV/c^2	6 MeV/c^2
$\Gamma(f_2(1270)\to\gamma\gamma)$	3.15 keV	0.07 keV
$M_{f_0(975)}$	1012 MeV/c^2	7 MeV/c^2
$\Gamma_{f_0(975)}$	52 MeV/c^2	20 MeV/c^2
$\Gamma(f_0(975)\to\gamma\gamma)$	0.29 keV	0.11 keV

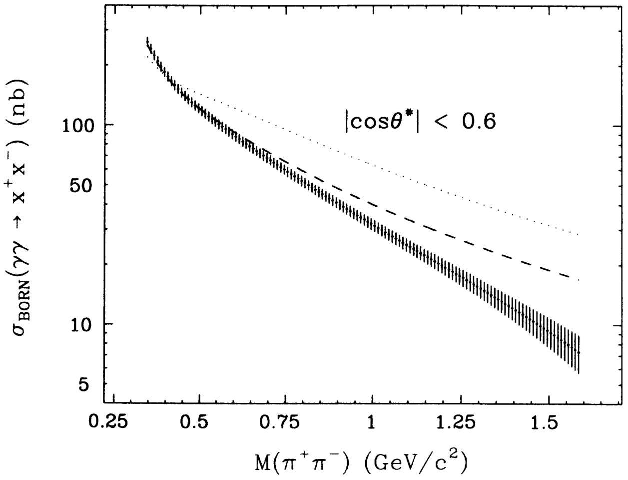

FIG. 17. The modified Born term. The points are the allowed values of $\mathcal{B}''_\lambda$ from a fit to our data. The dotted curve is the nominal Born term, and the dashed curve is $\mathcal{B}'_\lambda$, the Born term modified to reproduce the prediction of Ref. 15.

The mass dependence of the full width of the $f_2(1270)$ was parametrized in terms of an effective interaction radius r. For the above fit, we used $r=5.3\ (\mathrm{GeV}/c)^{-1}$. Hadronic scattering data allows us the freedom to vary r by $\pm1.2\ (\mathrm{GeV}/c)^{-1}$. Setting r at 6.5 and 4.1, we find that the fit for $\mathcal{B}''_\lambda$ changes by an amount that is small compared to the errors in Fig. 17. The radiative widths change by less than 2%, so that the systematic uncertainty due to setting $r=5.3\ (\mathrm{GeV}/c)^{-1}$ is negligible.

The errors on the radiative widths are strongly correlated with the full widths. To obtain a better estimate of the statistical error on the radiative widths, we fix the masses and full widths at their best values and then refit. The result is

$$\Gamma(f_2(1270)\to\gamma\gamma)=3.15\pm0.04\ \mathrm{keV}\ , \qquad \Gamma(f_0(975)\to\gamma\gamma)=0.29\pm0.07\ \mathrm{keV}\ . \tag{26}$$

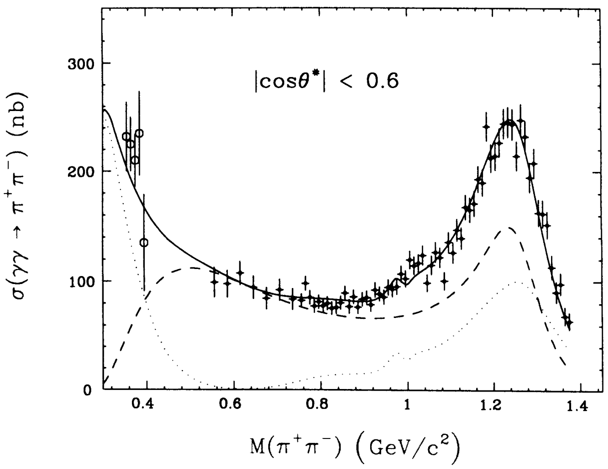

FIG. 18. A preferred solution of Morgan and Pennington superimposed on the data from this experiment. The dashed and dotted curves are respectively the helicity-2 and helicity-0 contributions.

Another check on the statistical significance of the $f_0(975)$ is made by refitting the data without the $f_0(975)$. The resulting χ^2 is worse by 20 for 3 fewer degrees of freedom, indicating that the statistical significance is approximately 4σ.

In the first attempt at a full amplitude analysis, Morgan and Pennington[15] have simultaneously fit the data from the reactions $\gamma\gamma \rightarrow \pi^+\pi^-$ (this experiment) and $\gamma\gamma \rightarrow \pi^0\pi^0$ (Crystal Ball)[11] with unitarized amplitudes constrained to the known $\pi^+\pi^-$ phase shifts. Ambiguities concerning the amount of S wave under the $f_2(1270)$ and the possible presence of broad scalar mesons limit their fits to families of solutions. The result of such a fit is shown in Fig. 18 together with our cross-section measurements. The several helicity components of the fit are also shown to indicate their importance in each mass region. Note that in addition to the $f_0(975)$ this fit contains significant S-wave components in the region of the

TABLE III. $\sigma(\gamma\gamma \rightarrow \pi^+\pi^-)$ in nanobarns, integrated over center-of-mass scattering angles, $|\cos\theta^*| < 0.6$. Statistical and systematic errors are given separately. The overall normalization error of $\sim 7\%$ (5% from luminosity and 5% from efficiency) is not included in the systematic errors.

$M_{\pi\pi}$ (GeV/c^2)	$\sigma(\gamma\gamma \rightarrow \pi^+\pi^-)$ (nb)	$M_{\pi\pi}$ (GeV/c^2)	$\sigma(\gamma\gamma \rightarrow \pi^+\pi^-)$ (nb)
0.355	232.0± 9.3±31.1	1.095	135.7± 9.5±4.5
0.365	225.0± 8.2±23.2	1.105	126.3± 9.3±4.3
0.375	210.0± 9.4±21.8	1.115	146.9±10.0±4.9
0.385	235.0±19.0±33.6	1.125	139.3± 9.8±4.7
0.395	135.0±25.4±35.8	1.135	167.6±11.3±5.7
0.555	99.2± 4.2±12.9	1.145	165.1±11.1±5.7
0.585	97.7± 3.6±11.8	1.155	170.8±11.5±5.9
0.615	107.5± 3.7±10.2	1.165	192.9±12.0±6.8
0.645	94.5± 3.4± 9.9	1.175	189.7±11.9±6.7
0.675	84.5± 3.3± 9.3	1.185	241.4±13.7±8.6
0.705	92.2± 3.6± 9.1	1.195	212.0±12.8±7.7
0.735	83.7± 3.5± 9.0	1.205	213.9±13.1±7.8
0.755	82.6± 6.1± 8.0	1.215	226.2±13.4±8.4
0.765	98.1± 6.5± 8.1	1.225	244.0±13.8±9.1
0.775	85.3± 6.2± 8.1	1.235	245.4±14.2±9.2
0.785	77.5± 6.0± 7.8	1.245	243.3±14.5±9.2
0.795	81.4± 6.2± 7.3	1.255	214.0±13.3±8.3
0.805	77.7± 6.1± 8.0	1.265	247.3±15.2±9.4
0.815	80.0± 6.1± 5.7	1.275	232.1±14.5±9.0
0.825	75.6± 5.8± 5.3	1.285	194.5±13.6±7.6
0.835	76.4± 6.0± 4.8	1.295	207.5±13.7±8.2
0.845	80.5± 6.1± 4.5	1.305	162.5±12.1±6.4
0.855	89.4± 6.3± 3.9	1.315	161.5±12.4±6.4
0.865	77.2± 6.3± 4.4	1.325	151.6±12.2±6.1
0.875	86.0± 6.4± 3.5	1.335	113.1±10.8±4.5
0.885	76.6± 5.9± 2.9	1.345	90.4± 9.6±3.7
0.895	83.8± 6.2± 3.0	1.355	97.8± 9.9±4.0
0.905	85.3± 6.3± 2.8	1.365	68.7± 8.1±2.9
0.915	78.8± 6.2± 2.7	1.375	64.2± 7.9±2.7
0.925	92.3± 6.8± 2.7	1.385	71.2± 8.5±3.0
0.935	88.7± 6.5± 2.8	1.395	63.6± 8.2±2.7
0.945	85.7± 6.6± 2.9	1.405	37.6± 6.5±1.7
0.955	94.7± 7.1± 2.8	1.415	45.2± 6.9±2.0
0.965	93.0± 7.0± 2.9	1.425	44.6± 6.7±2.0
0.975	95.4± 7.2± 3.0	1.435	36.1± 6.6±1.6
0.985	106.9± 7.5± 3.2	1.445	29.6± 6.1±1.3
0.995	102.6± 7.7± 3.4	1.455	26.1± 5.5±1.2
1.005	119.8± 8.3± 3.6	1.465	31.9± 6.4±1.4
1.015	114.4± 8.2± 3.6	1.475	16.1± 4.2±0.8
1.025	116.8± 8.2± 3.7	1.485	28.6± 6.2±1.3
1.035	123.9± 8.7± 3.9	1.495	27.3± 5.6±1.3
1.045	98.7± 7.8± 3.3	1.510	11.8± 2.7±0.6
1.055	114.9± 8.6± 3.7	1.530	13.4± 3.1±0.7
1.065	126.6± 9.1± 4.1	1.550	7.8± 2.3±0.5
1.075	122.0± 9.0± 4.0	1.570	10.8± 2.8±0.6
1.085	100.6± 8.1± 3.3	1.590	10.0± 2.6±0.6

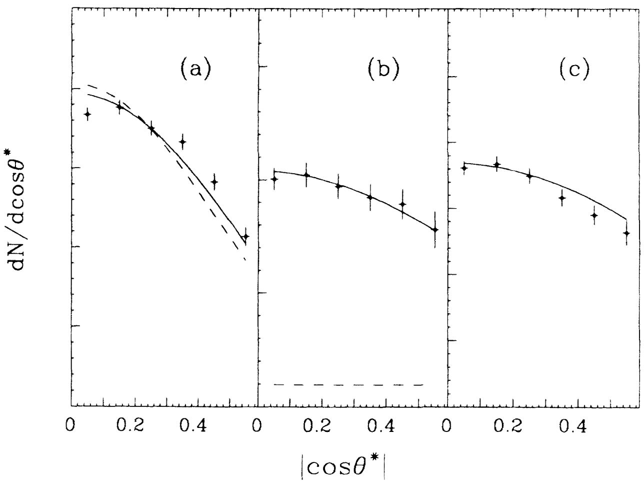

FIG. 19. Angular distributions: (a) near the $f_2(1270)$ [$1100<M(\pi^+\pi^-)<1400$ MeV/c^2]; (b) near the $f_0(975)$ [$980<M(\pi^+\pi^-)<1050$ MeV/c^2]; (c) below the $f_0(975)$ [$750<M(\pi^+\pi^-)<900$ MeV/c^2]. The solid curves are the fit from Table II. The dotted curve in (a) is the angular distribution for a helicity-0 $f_2(1270)$. The dashed curve in (a) shows the expected angular distribution if the ratio of the helicity-0 component of the $f_2(1270)$ amplitude to the helicity-2 component is $\frac{1}{2}$. The dashed line in (b) shows the contribution of the $f_0(975)$.

$f_2(1270)$. This has the additional effect of reducing the $f_2(1270)$ radiative width to 2.4 keV. The $f_0(975)$ radiative width remains near 0.5 keV for all their fits. Data at smaller center-of-mass angles would help in resolving these ambiguities.

E. Angular distributions

In fitting our data, we assumed that the $f_0(975)$ is a scalar and that the $f_2(1270)$ is produced in a pure helicity-2 state. We can check this by looking at the angular distributions. In Fig. 19, we show the angular distributions for three different mass regions. Table IV gives these angular distributions in finer detail. In the vicinity of the $f_0(975)$, the fit is very good. However, the $f_0(975)$ contributes only a small fraction of the cross section, so we are not very sensitive to its angular distribution.

In the region of the $f_2(1270)$, we fit to the angular distribution alone, assuming no scalar contribution, and fixing the contribution from the Born continuum at its fit value ($\mathcal{B}_\lambda''$ in Fig. 17). We define $\mathcal{F}_{f_2}^0$ and $\mathcal{F}_{f_2}^2$ as the helicity-0 and helicity-2 components of the amplitude for $\gamma\gamma\to f_2(1270)$:

$$\Gamma(f_2(1270)\to\gamma\gamma)\propto|\mathcal{F}_{f_2}^0|^2+|\mathcal{F}_{f_2}^2|^2 \ . \tag{27}$$

Fitting with statistical errors only, the best fit is for $\mathcal{F}_{f_2}^0=0$,with a 1σ upper limit on the ratio $\mathcal{F}_{f_2}^0$ to $\mathcal{F}_{f_2}^2$ of 0.12. Assuming no unitarization (which increases the contribution of the relatively isotropic Born continuum), we find that the upper limit increases to 0.18. If, as suggested by some authors,[15] there is a large scalar resonance underlying the $f_2(1270)$, then the limit is much larger. Without data at large $\cos\theta^*$, we cannot evaluate this possibility. Therefore, we quote our limit only under the assumption that no such scalar resonance contributes. Systematic uncertainties due to the shape of the continuum are comparable to the statistical uncertainties. Therefore, including systematic contributions of 0.09 from the unitarization question and 0.12 from the $\cos\theta^*$ dependence of the efficiency, we place a 1σ upper limit on the ratio:

$$\frac{|\mathcal{F}_{f_2}^0|}{|\mathcal{F}_{f_2}^2|}<0.20 \ . \tag{28}$$

Expressed as a 90% confidence limit on the ratio of the helicity components of the radiative width, Γ_λ, we may rewrite our limit, the most stringent to date, as

$$\frac{\Gamma_0(f_2(1270)\to\gamma\gamma)}{\Gamma_2(f_2(1270)\to\gamma\gamma)}<0.05 \text{ (90\% confidence level)} \ . \tag{29}$$

TABLE IV. $\sigma(\gamma\gamma\to\pi^+\pi^-)$ in nb, shown as a function of $\cos\theta^*$ in different regions of $M(\pi^+\pi^-)$. Only statistical errors are given.

$M_{\pi\pi}$ (GeV/c^2)	$\cos\theta$ 0.05	0.15	0.25	0.35	0.45	0.55
0.55–0.65	20.5±2.3	18.3±2.1	17.4±2.1	14.4±2.1	16.2±2.7	13.9±2.9
0.65–0.75	16.5±1.5	16.5±0.9	13.2±1.6	15.0±1.7	12.6±1.8	13.5±2.2
0.75–0.85	14.7±1.3	15.2±1.3	14.9±1.3	12.9±1.6	13.6±1.7	10.5±2.1
0.85–0.95	15.9±0.9	15.8±1.0	14.7±1.2	14.1±1.3	12.4±1.5	12.6±1.8
0.95–1.05	19.2±1.1	19.2±1.1	18.4±1.4	18.2±1.3	16.5±1.5	15.5±1.8
1.05–1.15	24.3±1.4	23.1±1.4	23.4±1.5	24.6±2.2	19.2±1.6	19.4±1.9
1.15–1.25	41.3±2.3	42.5±2.5	38.5±2.5	37.8±2.5	32.9±2.8	24.9±2.4
1.25–1.35	33.9±2.4	35.4±2.9	34.2±2.7	28.3±2.2	26.1±2.2	19.4±2.6
1.35–1.45	12.1±1.4	12.6±1.5	10.6±1.7	11.1±1.5	6.1±1.1	3.3±1.0
1.45–1.55	5.0±0.9	4.5±0.8	3.6±0.8	2.6±0.7	2.0±0.7	0.9±0.6

TABLE V. Systematic errors on $\Gamma(f_2(1270) \to \gamma\gamma)$ and $\Gamma(f_0(975) \to \gamma\gamma)$ considered in this analysis.

Systematic-error source	$\delta\Gamma(f_2(1270) \to \gamma\gamma)$	$\delta\Gamma(f_0(975) \to \gamma\gamma)$
$\delta\Gamma_R$ (full width)	5%	40%
$\delta\mathcal{E}$ (event efficiency)	5%	5%
$\delta\mathcal{L}$ (luminosity)	5%	5%
$\delta P_{\mathrm{ID}}(\pi)$ (pion identification)	4%	3%
	4%	3%
$\delta P_{\mathrm{ID}}(e,\mu)$ (leptonic subtraction)	2%	5%
	2%	5%
Hadronic backgrounds	< 1%	2%
Helicity hypothesis	2%	
Mass dependence of $\Gamma_{f_2(1270)}$	2%	2%
	2%	2%

We estimate the uncertainty in $\Gamma(f_2(1270) \to \gamma\gamma)$ due to the helicity-2 assumption by fitting with $\mathcal{F}^0_{f_2}$ fixed at its upper limit. This increases $\Gamma(f_2(1270) \to \gamma\gamma)$ by 2%.

F. Systematic errors

The relevant contributions to systematic uncertainties in the radiative widths of the $f_0(975)$ and the $f_2(1270)$ have been discussed as they arose. In Table V we list the systematic errors on $\Gamma(f_2(1270) \to \gamma\gamma)$ and $\Gamma(f_0(975) \to \gamma\gamma)$. The dominant contribution to the systematic uncertainty in the radiative width of the $f_0(975)$ is from the uncertainty in its full width (40% statistical). This could be reduced if we assume that the observed enhancement really is the $f_0(975)$, with mass shifted by some interference, and assume that its full width is that

TABLE VI. Measurements of $\Gamma(f_2(1270) \to \gamma\gamma)$. Models used to derive the results shown include (1) no interference (in which an interpolated smooth background was subtracted), (2) Born interference [in which the Born continuum was assumed to interfere with the $f_2(1270)$], (3) Mennessier (in which a program provided by Mennessier was used to enforce unitarity), and (4) Lyth (as described in this paper).

Experiment	Ref.	Model	Decay	$\Gamma(f_2 \to \gamma\gamma)$ (keV)
TASSO	6	No int.	$\pi^+\pi^-$	3.2±0.2±0.6
Crystal Ball (SPEAR)	9	No. int.[a]	$\pi^0\pi^0$	2.7±0.2±0.6
Crystal Ball (DORIS)	11 (prel.)	No int.[a]	$\pi^0\pi^0$	3.26±0.16±0.28
JADE	5 (prel.)	No. int.[a]	$\pi^0\pi^0$	3.09±0.10±0.39
Mark II (SPEAR)	10	Born int.[b]	$\pi^+\pi^-$	3.6±0.3±0.5
Mark II (PEP)	1	Born int.[c]	$\pi^+\pi^-$	2.52±0.13±0.38
Mark II (PEP)	This work	Born int.[d]	$\pi^+\pi^-$	2.80±0.04±0.28
DELCO	3	Born int.[e]	$\pi^+\pi^-$	2.70±0.05±0.2
DELCO	4 (unpub.)	Born int.[e]	$\pi^+\pi^-$	2.77±0.07±0.3
PLUTO	12	Born int.	$\pi^+\pi^-$	3.25±0.25±0.5
TPC/2γ	2	Born int.[b]	$\pi^+\pi^-$	3.2±0.1±0.4
PLUTO	12	Mennessier	$\pi^+\pi^-$	2.85±0.25±0.5
CELLO	7	Mennessier[e]	$\pi^+\pi^-$	2.5±0.1±0.5
CELLO	8 (prel.)	Mennessier[e]	$\pi^+\pi^-$	3.0±0.1±0.5
DELCO	4 (unpub.)	Mennessier	$\pi^+\pi^-$	2.93±0.07±0.29
DELCO	4 (unpub.)	Lyth	$\pi^+\pi^-$	3.34±0.07±0.34
Mark II (PEP)	This work	Lyth[d]	$\pi^+\pi^-$	3.15±0.04±0.31

[a] Measurements in the $\pi^0\pi^0$ channel are not as model dependent, because the nonresonant interfering continuum is much smaller.

[b] The interference between the Born term and the $f_2(1270)$ was multiplied by an arbitrary parameter, usually around 0.5.

[c] The QCD prediction of Brodsky and Lepage was used for $M(\pi^+\pi^-) > 1$ GeV/c^2.

[d] The Born term was modified to reflect the onset of a $1/s^3$ behavior expected from QCD in the vicinity of the $f_2(1270)$.

[e] The unpublished analysis is more recent than the published analysis, and is therefore assumed to supersede it.

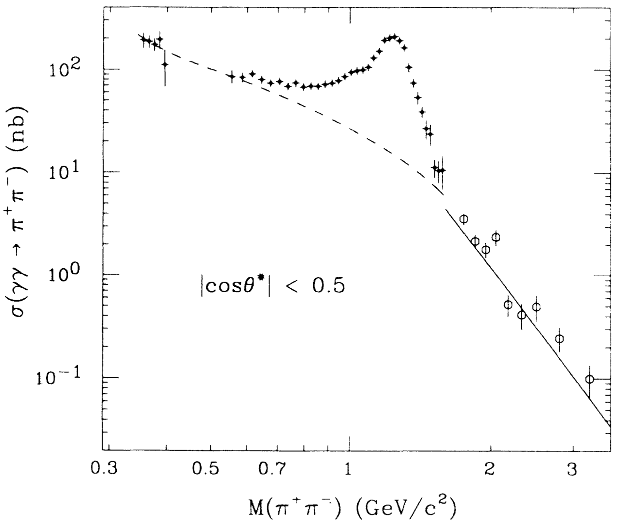

FIG. 20. Combined data from this analysis and previously published high-mass Mark II data. The large circles are the $\pi^+\pi^-$ cross section deduced from our measurement of the combined $\pi^+\pi^-$ and K^+K^- cross section under the hypothesis that the relative amounts of $\pi^+\pi^-$ and K^+K^- are accurately predicted in the model of Brodsky and Lepage. The solid line is the prediction of Brodsky and Lepage for pion pairs alone, and the dashed line is the modified continuum $\mathcal{B}_\lambda''$ from our best fit (Fig. 17). The angular region covered was limited to agree with that of the high-mass data.

listed in the Particle Data Group compilation:[29] $\Gamma_{f_0(975)}=34\pm6$ MeV. Because such a large mass shift is rather unlikely for such a narrow resonance, such a constraint is inappropriate.

The largest contribution to the uncertainty in $\Gamma(f_2(1270)\to\gamma\gamma)$ is from the unitarization scheme. This amounts to an uncertainty in the shape of the underlying continuum. Several other systematic errors listed in Table V contribute at the 5% level. Adding all the systematic errors in quadrature, we obtain the following results for the radiative widths:

$$\begin{aligned}\Gamma(f_2(1270)\to\gamma\gamma)&=3.15\pm0.04\pm0.39 \text{ keV} ,\\ \Gamma(f_0(975)\to\gamma\gamma)&=0.29\pm0.07\pm0.12 \text{ keV} .\end{aligned} \tag{30}$$

VII. CONCLUSIONS

We find that the reaction $\gamma\gamma\to\pi^+\pi^-$ is well described by the helicity-2 $f_2(1270)$ which interferes with the Born continuum, modified for final-state interactions. Another possible resonance at a mass of ~ 1010 MeV/c^2 was also observed. We find no evidence of low-mass resonances. In particular, we do not confirm previously reported enhancements,[12-14] but instead find agreement with the Born approximation below 500 MeV/c^2. For $M(\pi^+\pi^-)$ above 1 GeV/c^2, we corrected the Born term downward in order to obtain good agreement with our data. In Fig. 20, we show the data from this experiment together with our previous high-mass measurements.[31] This provides evidence that the correction was consistent with the gradual onset of a $1/s^3$ behavior, as predicted by Brodsky and Lepage[30] in the hard-scattering limit.

We observe a shoulder in the 1 GeV/c^2 region which we tentatively identify as the $f_0(975)$. This shoulder can be simply described as a scalar resonance with the parameters

$$\begin{aligned}M_{f_0}&=1010\pm7\pm10 \text{ MeV}/c^2 ,\\ \Gamma_{f_0}&=50\pm20\pm10 \text{ MeV}/c^2 ,\\ \Gamma(f_0\to\gamma\gamma)&=0.29\pm0.07\pm0.12 \text{ keV} .\end{aligned} \tag{31}$$

A similar shoulder at the 2σ level has been observed in the neutral channel ($\gamma\gamma\to\pi^0\pi^0$) by the Crystal Ball Collaboration.[11]

Originally, the $f_0(975)$ was thought to be a member of the $0^{++}q\bar{q}$ nonet. Some have speculated on the possibilities that it is a $K\bar{K}$ molecule, a 4-quark state, or a glueball. A review of these possibilities can be found in Ref. 32. Whatever its nature, its $\gamma\gamma$ width is an important probe of its parton content. In particular, most expectations are that a normal $q\bar{q}$ meson would have a radiative width of several keV, while more exotic states should have radiative widths that are smaller by about an order of magnitude. Our measured radiative width supports the latter hypothesis.

Our results on the radiative width of the $f_2(1270)$ are compared with those of other experiments in Table VI. Several models, most of which are designed to satisfy unitarity, have been used to fit the data and give radiative widths which vary by up to 20%. The fits of Morgan and Pennington indicate that the actual radiative width depends strongly on the assumed underlying S- and D-wave amplitudes. More complete angular coverage is needed to distinguish among the possible partial wave decompositions.

ACKNOWLEDGMENTS

We wish to thank Dr. D. Morgan and Dr. M. Pennington for many helpful discussions. This work was supported in part by the U.S. Department of Energy Contracts No. DE-AC03-76F00515 (SLAC), No. DE-AC03-76SF0098 (LBL), and No. DE-AC02-76ER03064 (Harvard University).

(a)Present address: Columbia University, New York, NY 10027.

(b)Present address: University of Oklahoma, Norman, OK 73019.

(c)Present address: University of Chicago, Chicago, IL 60637.

(d)Present address: Harvard University, Cambridge, MA 02138.

(e)Present address: Therma-Wave Corp., Fremont, CA 94539.

(f)Present address: Brookhaven National Laboratory, Upton, NY 11973.

(g)Present address: Fermi National Laboratory, Batavia, IL 60510.

(h)Present address: California Institute of Technology, Pasadena, CA 91125.

(i)Present address: University of Illinois, Urbana, IL 61801.

(j)Present address: CERN, CH-1211, Geneva 23, Switzerland.

(k)Present address: University of California, Santa Cruz, CA 95064.

(l)Present address: University of Pennsylvania, Philadelphia, PA 19104.

(m)Present address: Carleton University, Ottawa, Ontario, Canada, K1S 5B6.

(n)Present address: University of Florida, Gainesville, FL 32611.

(o)Present address: University of Geneva, CH-1211, Geneva 4, Switzerland.

[1] Results on the first 35 pb^{-1} of this experiment have been published in J. R. Smith *et al.*, Phys. Rev. D **30**, 851 (1984).

[2] TPC/2γ Collaboration, H. Aihara *et al.*, Phys. Rev. Lett. **57**, 404 (1986).

[3] DELCO Collaboration, A. Courau *et al.*, Phys. Lett. **147B**, 227 (1984).

[4] DELCO Collaboration, R. Johnson, Ph.D. thesis, Report No. SLAC 294.

[5] JADE Collaboration, J. E. Olson, in *Proceedings of the 24th International Conference on High Energy Physics,* Munich, West Germany, 1988, edited by R. Kotthaus and J. Kuhn (Springer, Berlin, 1988).

[6] TASSO Collaboration, R. Brandelik *et al.*, Z. Phys. C **10**, 117 (1981).

[7] CELLO Collaboration, H. J. Behrend *et al.*, Z. Phys. C **23**, 223 (1984).

[8] CELLO Collaboration, H. J. Behrend *et al.*, in *Proceedings of the 24th International Conference on High Energy Physics* (Ref. 5).

[9] Crystall Ball Collaboration, C. Edwards *et al.*, Phys. Lett. **110B**, 82 (1982).

[10] Mark II Collaboration, A. Roussarie *et al.*, Phys. Lett. **105B**, 304 (1981).

[11] Crystal Ball Collaboration, H. Marsiske *et al.*, Phys. Rev. D **41**, 3324 (1990); in *Proceedings of the XXIII International Conference on High Energy Physics,* Berkeley, California, 1986, edited by S. C. Loken (World Scientific, Singapore, 1987), p. 1223. Also H. Marsiske, Ph.D. thesis, Hamburg Report No. DESY-F31-88-02, 1988.

[12] PLUTO Collaboration, Ch. Berger *et al.*, Z. Phys. C **26**, 199 (1984).

[13] DM1 Collaboration, A. Courau *et al.*, Nucl. Phys. **B271**, 1 (1986).

[14] DM2 Collaboration, Z. Ajaltouni *et al.*, Phys. Lett. B **194**, 573 (1987).

[15] D. Morgan and M. R. Pennington, Phys. Lett. B **192**, 207 (1987); Z. Phys. C **37**, 431 (1988); and (private communication).

[16] G. Mennessier, Z. Phys. C **16**, 241 (1983).

[17] D. H. Lyth, J. Phys. G **10**, 39 (1984).

[18] R. H. Schindler *et al.*, Phys. Rev. D **24**, 78 (1981).

[19] D. Karlen, Mark II memo, 1987 (unpublished).

[20] P. C. Rowson, Ph.D. thesis, Report No. LBL-20463, 1985.

[21] GGDEPA is based on S. J. Brodsky, T. Kinoshita, and H. Terazawa, Phys. Rev. Lett. **25**, 972 (1970); Phys. Rev. D **4**, 1532 (1971).

[22] F. M. Renard, *Electron Positron Collisions* (Editions Frontières, Gif-sur-Yvette, France, 1981), p. 206.

[23] F. A. Berends, P. H. Daverveldt, and R. Kleiss, Leiden report (unpublished); see also Phys. Lett. **148B**, 489 (1984).

[24] H. D. I. Arbanel and M. I. Goldberger, Phys. Rev. **165**, 1594 (1968).

[25] V. M. Budnev *et al.*, Phys. Rep. C **15**, 241 (1975).

[26] K. M. Watson, Phys. Rev. **88**, 1163 (1952).

[27] J. M. Blatt and V. F. Weiskopf, *Theoretical Nuclear Physics* (Wiley, New York, 1952), pp. 359–365 and 386–389.

[28] G. Grayer *et al.*, Nucl. Phys. **B75**, 189 (1974).

[29] Particle Data Group, G. P. Yost *et al.*, Phys. Lett. B **204**, 1 (1988).

[30] S. J. Brodsky and G. P. Lepage, Phys. Rev. D **24**, 1808 (1981).

[31] J. Boyer *et al.*, Phys. Rev. Lett. **56**, 207 (1986).

[32] M. S. Chanowitz, in *Photon-Photon Collisions,* proceedings of the VIIIth International Workshop, Shoresh, Israel, 1988, edited by Uri Karshon (World Scientific, Singapore, 1989).